

Development and application of a microstructure-based approach to characterize and model failure initiation in DP steels using XFEM

A. Ramazani ^{a,*}, M. Abbasi ^b, S. Kazemiabnavi ^c, S. Schmauder ^d, R. Larson ^a, U. Prahl ^e

^a Department of Chemical Engineering, University of Michigan, 2300 Hayward St., Ann Arbor, USA

^b Faculty of Engineering, University of Kashan, Ravandi Blvd, Kashan, Iran

^c Department of Mechanical Engineering, University of Michigan, 2300 Hayward St., Ann Arbor, USA

^d Institute of Materials Testing, Materials Science and Strength of Materials, University of Stuttgart, Pfaffenwaldring 32, Stuttgart, Germany

^e Department of Ferrous Metallurgy, RWTH Aachen University, Intzestr.1, D-52072 Aachen, Germany

ARTICLE INFO

Article history:

Received 15 July 2015

Received in revised form

19 February 2016

Accepted 29 February 2016

Available online 3 March 2016

Keywords:

Dual-phase (DP) steel

Representative volume element (RVE)

Dislocation-based model

Flow curves of single phases

Extended finite element method (XFEM)

ABSTRACT

We develop a microstructure-based model to characterize and model failure initiation in DP steels using an extended finite element method (XFEM) to simulate martensite cracking on the mesoscale combined with representative volume element (RVE) modeling. A mini tensile test with digital image correlation (DIC) analysis is linked to local SEM analysis to identify the local strain at which failure is initiated. In-situ bending tests in SEM with electron backscatter diffraction (EBSD) measurements before and after the test are carried out to validate that the crack initiates in the martensite islands. Empirical equations for XFEM parameters as functions of local carbon content in martensite are fit to experimental results for laboratory-annealed DP600 steels with varying martensite content. The equations are then shown to predict successfully failure initiation in industrially produced DP steels with various chemistries, strengths and martensite fractions.

© 2016 Elsevier B.V. All rights reserved.

1. Introduction

Dual-phase (DP) steels show a combination of high strength with good ductility [1–4]. These desirable properties are attributed to the microstructure of DP steel, which normally consist of hard martensite particles dispersed in a soft ferrite matrix [5–7]. Therefore, DP steels are widely used in industry, especially for automotive structural and safety parts. Recent studies have shown that in future cars, DP steels may account for up to 80% of the total weight. For instance, DP600 is used in the dash cross member, B-pillar and front rail closeout [8–12]. However, application of DP steels is currently restricted due to their complex failure behavior, arising from the microstructure of these materials. Therefore, much current research is focused on the failure behavior of DP steels.

Although at the macroscopic scale DP steel exhibits uniform and homogenous deformation, due to its grain-level inhomogeneity, the microscopic deformation is non-uniform. At the macroscopic level, DP steels fail in a ductile manner, which can be divided into three stages: void nucleation, void growth and void coalescence. In microscopic level, three competitive failure modes

for failure initiation of DP steels have been demonstrated: brittle fracture (martensite cracking); ferrite/martensite interface decohesion, and ductile degradation of the ferrite matrix [13–19]. Ahmed et al. [20] reported that void formation occurred due to ferrite–martensite interface decohesion at low to intermediate martensite volume fractions ($V_m < 0.32$), while at higher V_m it is due to martensite particle cracking. Consistent with this, Gurland [21] found that void formation occurs due to ferrite/martensite interface decohesion in DP steels with V_m equal 0.16. Speich and Miller [22] reported that at high V_m , martensite cracking is the main failure mechanism, which is again consistent with the work of Ahmed et al. [20].

Going beyond the effect of V_m , He et al. [23] studied the effect of martensite morphology (i.e., the size/aspect ratio of martensite islands) on the fracture mechanism in DP steel. Their results indicated that the coarse morphology of martensite (large size, elongated shape, and geometrical distribution along the ferritic grain boundaries) restricted plastic flow of the ferrite grains, causing a high stress, which initiated cracking in martensite islands. However, when plastic deformation became severe, a transition from martensite cracking to interfacial decohesion at the ferrite/martensite interface was observed [23]. On the contrary, with finely dispersed martensite microstructure, the voids mainly formed at the ferrite/martensite interface [23]. Kim and Thomas

* Corresponding author.

E-mail address: ramazani@umich.edu (A. Ramazani).

[24] also correlated the formation of voids in dual-phase steels with martensite morphology. Consistent with the findings of He et al. [23], Kim and Thomas [24] found that for coarse martensite islands the failure occurred by cracking, while for finely distributed martensite the void initiation occurred by de-bonding at the ferrite/martensite interface. Shen et al. [14] used a scanning electron microscope (SEM) equipped with a tensile straining stage to illustrate the inhomogeneous strain distributions between ferrite and the martensite grains in DP steels. According to their investigation, the ferrite phase starts to deform immediately after imposition of macroscopic deformation, and at a much higher rate than the martensite phase. They also concluded therefore that the volume percentage of martensite in the DP steel influences the failure mechanism. Calcagnotto et al. [25] investigated the mechanical properties and failure behavior of DP steels with different grain sizes (coarse grain, fine grain, and ultrafine grain) performing mini tensile tests using digital image correlation (DIC). They showed that refining the ferrite grains modifies the tensile strength of DP steels without any effects on the ductility and failure strain of the material. They stated that failure is caused by martensite cracking in coarse grained DP steels, while grain boundaries play the most significant role in the failure initiation of DP steels with fine and ultra fine ferrite grains. Ramazani [26] showed martensite cracking occurred as well as ferrite/martensite debonding in DP steels with fine and ultrafine grains. He simulated martensite cracking in DP steels studied by Calcagnotto et al. [25], and found very good agreement between experimental and simulation results.

A number of publications show that micromechanical modeling can give predictions that compare well to the experimental results. Sun et al. [27] predicted the ductile failure and ductility of DP steels, assuming that failure occurs by plastic strain localization resulting from the incompatible deformation between the hard martensite and soft ferrite matrix. In their work, 2D representative volume elements (RVE) from an SEM image were utilized to do regular 2D finite element calculations. Uthaisangsuk et al. [28] investigated the failure of DP steels using RVE approach as well. They utilized a cohesive zone and Gurson–Tvergaard–Needleman model (GTN) models to study the ferrite/martensite debonding and ferrite degradation, respectively. Concerning the modeling of martensite cracking, three alternatives can be considered. First, the Beremin local criterion can be used, which is based on a statistical concept with a Weibull modulus to describe the probability of fracture in terms of a local failure stress [29]. Cohesive zone model can also be utilized for modeling brittle fractures in steels [30]. This model defines cohesive interface elements between continuum elements, which open and lose their stiffness when damage occurs. Therefore, the crack can only propagate along these cohesive elements and, consequently, the direction of crack propagation must be predefined when using the cohesive zone model. Finally, with the XFEM technique, there is no need to predefine the direction of crack propagation because crack will be generated within the interior of a FE element [31]. A traction separation law for the stiffness degradation of an element similar to the cohesive zone model is applied for the case of XFEM. Vajragupta et al. [32] employed two different damage mechanics methods to study the interaction between failure modes in DP steels by means of RVE, namely: 1) XFEM to track the damage onset and progression in martensitic regions, and 2) a damage curve for the ductile ferritic phase. These two local damage models were combined into an RVE model that predicted the failure of the material as a whole, with debonding neglected. Zhuang et al. [33], on the other hand, predicted the failure of DP590 steel using an RVE model with plastic strain localization (or shear banding) in the ferrite triggered by the irregular domain structure. When the banding became severe, they presumed that decohesion between martensite and

ferrite would occur. Their results showed that the strain localization caused by the martensite inclusions provides the source for failure initiation. Ramazani et al. [34–37] characterized and model the effect of microstructural features on the failure initiation in DP600 steels. For instance, in [36] they investigated the effect of martensite morphology on the failure initiation of DP600 steel. They showed that martensite cracking was the main failure initiation mechanisms in equiaxed and banded DP steels. However, failure initiation occurred in the equiaxed microstructure in the higher plastic strain compared to the banded microstructure. Therefore, DP steel with equiaxed microstructure shows better failure behavior than a banded one does, while failure initiated in both microstructures due to the same mechanism. They used XFEM, which is appropriate when martensite cracking is the main failure initiation mechanism, and investigated the effect of compositional heterogeneity (i.e., martensite banding) on the failure initiation of DP steels [36].

As mentioned above, DP steels are prone to two different fracture mechanisms: martensite cracking and martensite-ferrite interface decohesion. The relative activity of these mechanisms is strongly dependent on microstructural parameters and microstructural heterogeneity. Tasan et al. [38] examined the dependence of martensite cracking and martensite-ferrite decohesion on ferrite grain size and martensite fraction. Based on their observations, for high ferrite grain sizes and small martensite content, the interface damage mechanism is dominant, while for high martensite content and low ferrite grain size, martensite cracking is promoted. Nowadays because of high mechanical demands of industries, DP steels with low ferrite grain size (lower than 20 μm) and martensite content of 20–40 (%) predominate [39]. For these kinds of steels both fracture mechanisms have been reported [38]. Therefore, another parameter besides ferrite grain size and martensite content must control the failure initiation in these materials. Here, we introduce martensite carbon concentration as a crucial parameter, which we believe plays the key role on the mechanical properties and failure initiation of DP steels. Thus, both failure mechanisms (i.e., martensite cracking and interface debonding) should be formulated as a function of martensite carbon content. XFEM with a traction-separation law and cohesive zone models are typically used to simulate martensite cracking and ferrite-martensite debonding, respectively. In this work, we formulate XFEM parameters for traction-separation as a function of martensite carbon content and validate them for industrially produced DP qualities with various chemistries, strength levels and martensite phase fractions. We will formulate cohesive zone model parameters as a function of martensite carbon content to simulate martensite-ferrite debonding in DP steels in the next work. We expect to be able to evaluate dominant failure mechanisms for failure initiation in DP steels by calculating the critical energy for both martensite cracking and ferrite/martensite interface debonding.

In the current research work, a microstructure-based failure model will be developed, applied and generalized to quantify to characterize and model failure initiation in DP steels. Specifically, laboratory-annealed samples with DP600 chemistry with varying martensite content were created by controlling the heat-treatment parameters. RVEs were deformed numerically using Abaqus software, implementing XFEM while the dislocation-based theory was applied to model the flow behavior of DP600 steel constituents and a traction separation law was used as the damage criterion. Martensite cracking is thereby found to be the primary mechanism for crack initiation, and relevant equations are developed for damage model parameters of martensite, namely strength and energy, as a function of carbon content. Subsequently, RVEs of the DP500, DP800 and DP1000 steels were stretched numerically and the proposed equations were applied to obtain 2D flow curves. 2D

flow curves of steels were then correlated to 3D flow curves using a 2D–3D correlation equation presented in Ref. [40]. Finally, failure initiation in industrially produced DP steels with various chemistries, strength levels and martensite fractions were investigated using the equations relating damage parameters (strength and energy) to carbon content. Our results suggest that carbon content may be as important to failure as grain size and martensite fraction, at least for some DP steels.

2. Materials and methods

2.1. Materials

In the current research, four kinds of DP steels were considered: DP500, DP600, DP800 and DP1000 steels. Laboratory heat treatment was performed on DP600 steel to create DP steels with varying martensite/ferrite fraction and ferrite grain size. Sheets of DP600 steel were immersed in a salt bath at three different temperatures: 740, 760 and 780 °C with a holding time of 5 min. Finally, the samples were quenched in water to room temperature, which led to the transformation of austenite to martensite. More information about the applied heat treatment can be found in Ref. [26]. The chemical compositions of the investigated steels were determined using optical emission spectroscopy and are presented in Table 1.

2.2. Microstructural characterization

3% Na₂S₂O₅ solution was applied as an etchant with an etching time of about 30 s. Martensite particle size and aspect ratio were measured using a Digimizer program, as explained in [1]. The linear intercept method based on ASTM-E112 standard test [41] was applied to determine the ferrite grain size. Additionally, electron backscatter diffraction (EBSD) was used for phase identification, grain boundary and morphology studies. The equipment used for EBSD measurements is presented in Table 2. Detailed information can be found in [42].

The carbon content of ferrite (C_{α}) was approximated using ThermoCalc software with the TCFE6 database. The following elements were taken into account for ThermoCalc calculations: Mn, C, Si, Cr and Ni. The carbon content of the martensite (C_m) was calculated by considering the carbon mass balance and based on the following relation:

$$C_{DP} = C_{\alpha}V_{\alpha} + C_mV_m \quad (1)$$

where V_{α} , and V_m , are ferrite and martensite volume fractions, measured experimentally based on the ASTM-E562 standard [43], respectively. C_{DP} stands for the nominal carbon composition of the DP steel, determined through optical emission spectroscopy, as mentioned in Section 2.1.

2.3. Tensile test and mini tensile test with DIC technique

Tensile tests based on DIN EN10002 [44] were performed parallel to the cold-rolling direction at a velocity of 4 mm/min at

Table 2

Equipment used for EBSD measurements.

The EBSD machines	SEM: JEOM JSM 7000F
EBS detector	Digiview III by EDAX-TSL
Data acquisition software	OIM data collection and OIM analysis

the Zwick 100. To identify the failure initiation position precisely and the corresponding local strain, we used digital image correlation (DIC), which is a full-field image analysis method that quantitatively determines the contour of the bar, deformation and strain on the surface of the specimen [45]. After removing the impurities and dust from the surfaces of the samples, the samples were colored white to provide a uniform, contrasting background, against which a pattern of black spots was sprayed. A high speed camera was set in the front of the sample on a stable tripod to track these spots during deformation and correspondingly to measure the true strain over the whole area. More information about the procedure followed can be found in Ref. [26].

2.4. In-situ bending test with EBSD measurement

In-situ three-point-bending tests were carried out at room temperature in order to determine the failure initiation site in DP600 steels. The bending test procedure and the sample geometry are schematically shown in Fig. 3. The rolling direction was aligned with the major stress direction. The SEM was adjusted to obtain an image with appropriate brightness and contrast, focusing on the area between two pre-existing notches in both sides. A displacement-controlled load was applied to the samples to evaluate the process of crack initiation, with deflection and load recorded automatically. Additionally, SEM photos were taken at any moment when changes of mesoscale structure or damage growth occurred in the specimen. Hence, the mechanical loads at the initiation of crack formation and the location of crack initiation were identified precisely. Additionally, EBSD measurements were made before and after the test to identify which phase or interphase fails first.

3. Micromechanical modeling

3.1. RVE generation

A 2D representative volume element (RVE), which is intended to be representative of the entire sample, was first created from the microstructures of all studied DP steel. Selected areas of light optical microscopy (LOM) images of the experimental microstructure were converted into a 2D RVE, taking advantage of the color difference between martensite and ferrite, using an in-house finite element generator, Gitter. The smallest satisfactory dimension of the RVE in DP steels is $24 \times 24 \mu\text{m}^2$, which should contain a minimum of 19 martensite particles, as reported by Ramazani et al. [46]. The RVE size therefore was taken of $40 \mu\text{m} \times 40 \mu\text{m}$, $32 \mu\text{m} \times 32 \mu\text{m}$, and $40 \mu\text{m} \times 40 \mu\text{m}$ for DP steel with 20%, 37% and 46% martensite, respectively. Plane strain elements (CPE4R) were

Table 1

The chemical composition of the investigated steels (wt%).

	C	Si	Mn	P	S	Cr	Ni	Al	Cu	V
DP500	0.071	0.096	1.42	0.016	0.001	0.48	0.023	0.034	0.013	0.007
DP600	0.072	0.24	1.58	0.015	0.001	0.55	–	0.032	–	–
DP800	0.116	0.23	1.41	0.013	0.001	0.02	0.034	0.032	0.006	0.017
DP1000	0.142	0.53	1.40	0.009	0.002	0.016	0.03	0.039	0.02	0.008

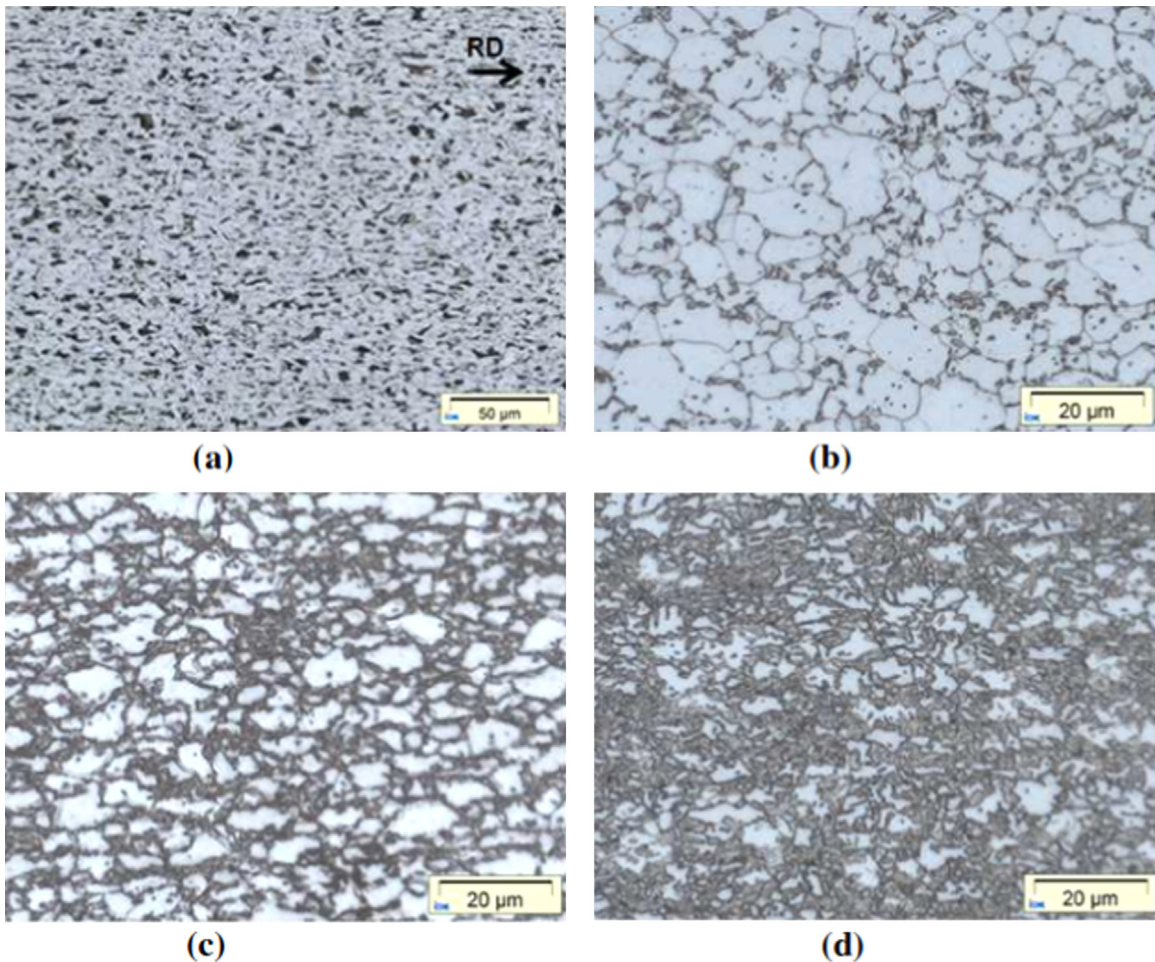


Fig. 1. As-received microstructures of the various studied steels. a) cold-rolled DP600, b) DP500, c) DP800 and d) DP1000.

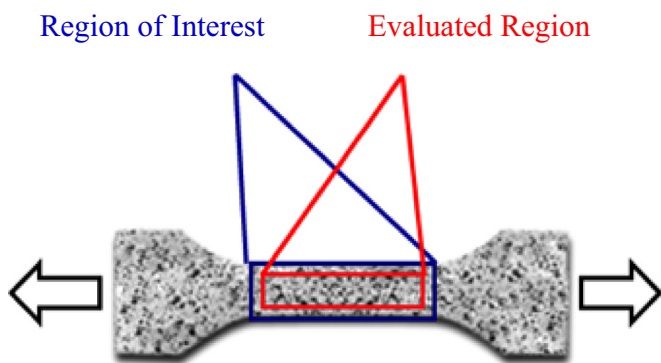


Fig. 2. Illustration of the black spots formed on the white surface of tensile test specimen. The region evaluated during the tensile test is shown.

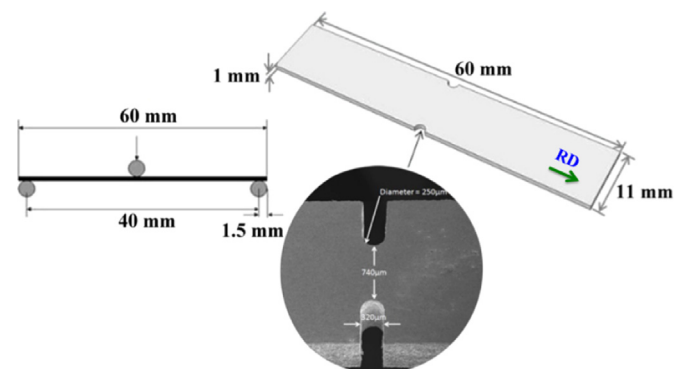


Fig. 3. Schematic design of bending test as well as geometry of workpiece and tools. "RD" is the rolling direction.

Table 3
Volume fraction of martensite phase (V_m), ferrite grain size, austenization temperature (TA), carbon content of ferrite (C_α) and austenite (C_γ) for the studied steels.

Steel	TA (°C)	Ferrite grain size (μm)	V_m (vol%)	C_α (wt%)	C_γ (wt%)
DP600	740	4.43	20	0.0066	0.334
DP600	760	3.76	37	0.0049	0.186
DP600	780	3.21	46	0.004	0.151
DP500	760	5.42	15	0.0028	0.457
DP800	760	4.74	30	0.0037	0.378
DP1000	780	3.96	50	0.0033	0.281

employed for the numerical tensile tests. Additionally, the effect of mesh size was studied in a previous study [40] with ranging element length from 0.1 to 2 mm, and no deviation was obtained for the meshes finer than 0.25 mm. Therefore, in the current study, quadratic meshes with element size of 0.25 mm were used for the modeling.

3.2. Single phase flow curve modeling

In the current work, the elastic modulus for ferrite and martensite is assumed to be 210 GPa [40]. A dislocation-based strain-hardening model [47] was applied to define the flow curve of

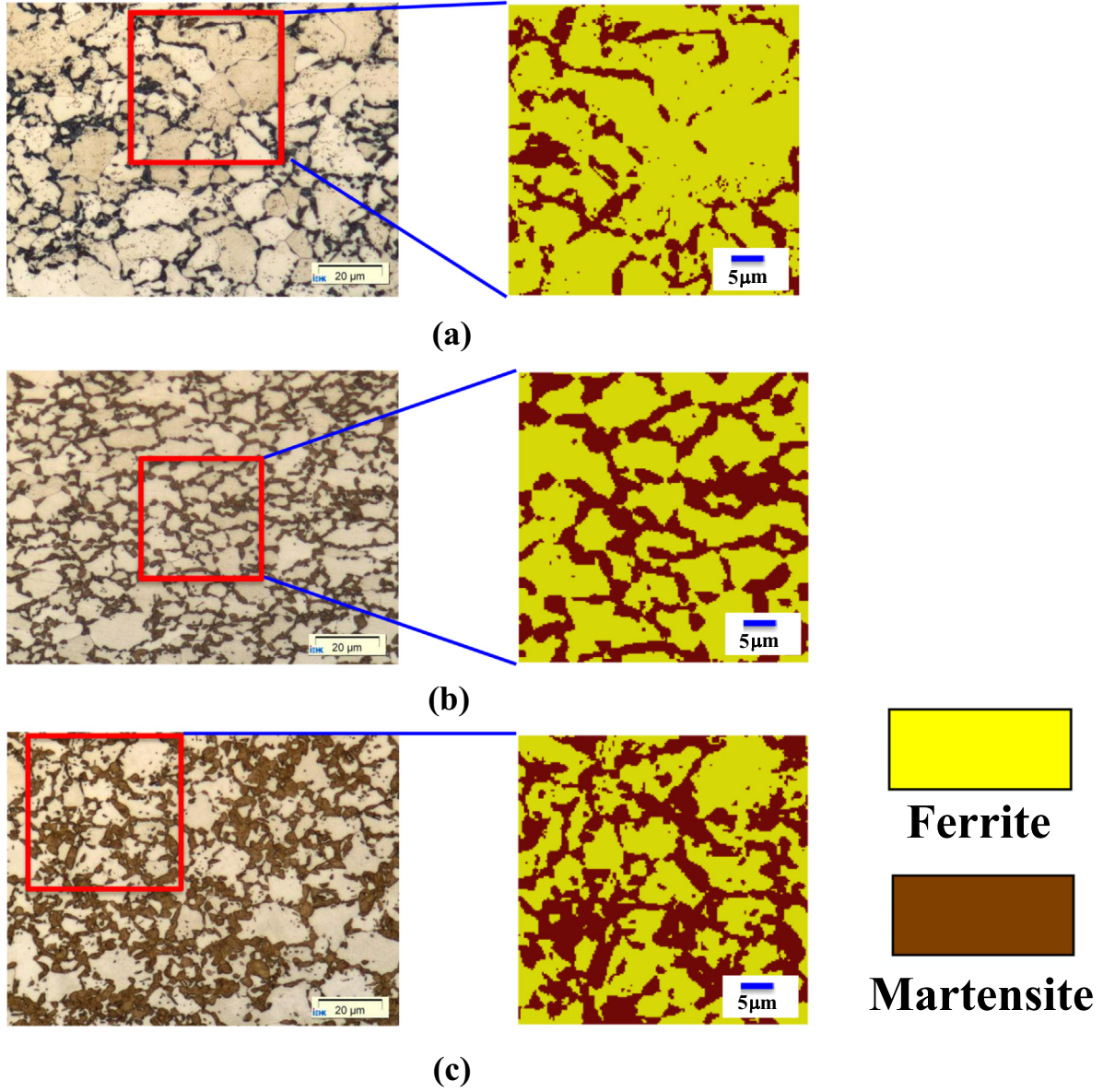


Fig. 4. Presentation of LOM microstructures and the created RVEs (contained in the red boxes) for DP600 steels with different volume fractions of martensite: (a) 20% (RVE size is $40 \mu\text{m} \times 40 \mu\text{m}$), (b) 37% (RVE size is $32 \mu\text{m} \times 32 \mu\text{m}$) and (c) 46% (RVE size is $40 \mu\text{m} \times 40 \mu\text{m}$). (For interpretation of the references to color in this figure legend, the reader is referred to the web version of this article.)

individual phases for ferrite and martensite (Eq. (2)). This model emerges from the classical dislocation theory approach of [48,49] and from the work of [50].

$$\sigma(\text{in MPa}) = \sigma_0 + \Delta\sigma + \alpha * M * \mu * \sqrt{b} * \sqrt{\frac{1 - \exp(Mk_r \epsilon)}{k_r * L}} \quad (2)$$

where σ and ϵ are the flow stress (von Mises stress) and true strain (equivalent plastic strain), respectively. In the above relation, the first term σ_0 describes the effect of the Peierls stress and of the alloying elements in the solid solution [47].

$$\sigma_0(\text{in MPa}) = 77 + 750(\%P) + 60(\%Si) + 80(\%Cu) + 45(\%Ni) + 60(\%Cr) + 80(\%Mn) + 11(\%Mo) + 5000(\%N_{ss}) \quad (3)$$

The second term in Eq. (2) accounts for strengthening by carbon in solution, which for ferrite is:

$$\Delta\sigma(\text{in MPa}) = 5000 * (\%C_{ss}^f) \quad (4)$$

And in the case of martensite it is:

$$\Delta\sigma(\text{in MPa}) = 3065 * (\%C_{ss}^m)^{-161} \quad (5)$$

The third term accounts for strengthening by dislocation density, precipitation hardening, grain size as well as work softening due to recovery. According to Ref. [51,52], α is a constant with a value of 0.33. M is the Taylor factor with a value of 3. μ is the shear modulus with a value of 80,000 MPa. b is the Burger's vector (2.5×10^{-10} m). k is the recovery rate and in the case of ferrite a value of $10^{-5}/d_\alpha$ is assumed, where d_α refers to the ferrite grain size. For martensite, the k value is 41. L is the dislocation mean free path. For ferrite it is the same as the grain size (d_α), while for martensite it is a constant with a value of 3.8×10^{-8} m [51,52].

3.3. Extended finite element method (XFEM) and parameters identification

XFEM with a traction separation law was utilized to model the failure initiation. The initiation and propagation of cracks under

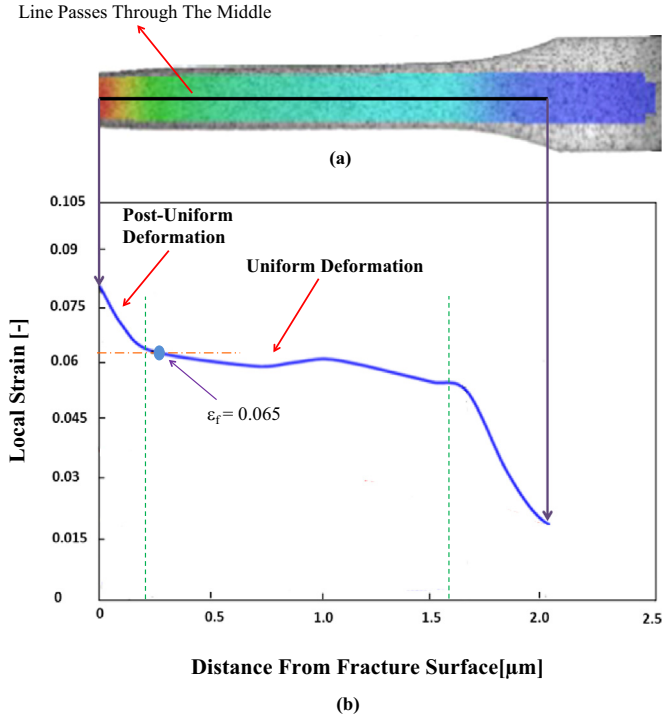


Fig. 5. (a) Strain distribution for DP600 steel with 46% martensite resulting from the tensile test with DIC, (b) strain-distance curve relevant to the depicted strain distribution. The failure initiation strain is marked as ϵ_f .

Table 4

Values of traction separation model parameters for DP600 steels with different martensite volume fractions (V_m). ϵ_f and ϵ_f^m denote the local failure strain in the material, determined by the tensile test with DIC as shown in Fig. 5, and in the martensite, determined by RVE simulations. σ_c and E_c are the critical strength and energy of martensite from the simulations and martensite flow curve, Eq. (2), and C_{ss}^m is the carbon content of martensite, obtained from THERMOcalc.

DP600	ϵ_f	ϵ_f^m	σ_c (MPa)	E_c (MPa)	$\%C_{ss}^m$
$V_m=20\%$	0.086	0.028	2140	25.11	0.342
$V_m=37\%$	0.079	0.023	1660	19.32	0.189
$V_m=46\%$	0.065	0.018	1525	17.39	0.154

quasi-static conditions were studied using XFEM because it allows crack growth along an arbitrary, solution-dependent path without re-meshing the FE domain [53]. Therefore, the FE results of crack initiation and crack growth are strongly mesh-dependent. To ease this problem, the extended finite element method (XFEM), which also allows the application of stress based criteria, was introduced [54,55].

XFEM introduces a priori knowledge about failure modes into the approximation space through the addition of “enrichment functions”. It enables, thereby, the accurate approximation of fields that involve jumps, kinks, singularities, and other non-smooth features within elements. The enrichment functions consist of the near-tip asymptotic displacement functions, which describe the singularity around the crack tip and a discontinuous function that represents the jump in displacement across the crack surfaces. Then, the approximation for a displacement vector function u is obtained by “partitioning the unity enrichment” as follows [54,55]:

$$u = \sum_{l=1}^N N_l(x)[u_l + H(x)a_l] + \sum_{\alpha=1}^4 F_{\alpha}(x)b_l^{\alpha} \quad (6)$$

where $N_l(x)$ are the usual nodal shape functions; the first term on the right-hand side of the above equation, u_l , is the usual nodal

displacement vector associated with the continuous part of the finite element solution; the second term is the product of the nodal enriched degree of freedom vector, a_l , and the associated discontinuous jump function $H(x)$ across the crack surfaces; and the third term is the product of the nodal enriched degree of freedom vector, b_l^{α} , and the associated elastic asymptotic crack-tip functions, $F_{\alpha}(x)$. The first term on the right-hand side is applicable to all the nodes in the model; the second term is valid for nodes whose shape function support is cut by the crack interior; and the third term is used only for nodes whose shape function support is cut by the crack tip. More details can be found in [37].

The maximum principle stress criterion (MAXPS) using critical failure stress (σ_c) and failure energy (E_c) was applied to describe damage initiation. Martensite is assumed to lose its stiffness as soon as the damage initiation criterion is reached and linear degradation behavior with steep slope is assigned as local damage evolution law on mesoscale [35]. For this purpose, the corresponding local strain for failure initiation in DP steels in mini tensile tests with DIC technique was first determined. Micro-mechanical modeling based on 2D RVE calculations was performed in order to identify the average equivalent strain in martensite when the crack initiation occurs. Therefore, the simulations were conducted up to the determined local failure strains from the experiments. Then, using first order homogenization strategy [56], average equivalent plastic strain in martensite was calculated. The corresponding stress for this strain can be considered as critical stress for martensite cracking, σ_c , and it was calculated from the flow curve of martensite according to fracture toughness theory [57], critical failure energy for martensite failure, E_c , was calculated from the martensite stress-strain curve.

Using these damage model parameters for DP600 steels, crack-initiation equations were developed for maximum stress and fracture energy parameters of the damage model; these equations will be given below. To test and generalize these 2D RVEs of three other industrially produced DP steels, DP500, DP800 and DP1000, were stretched numerically using Abaqus with XFEM while the values for damage model parameters were obtained from the crack initiation equations developed for the laboratory-generated steel DP600. Simulations were carried out and the 2D flow curves of the studied steels were obtained.

3.4. Correlation between 2D and 3D flow curve modeling

Since real specimens deform three-dimensionally, 2D modeling approaches cannot predict the flow curve of the material precisely. The predicted flow curves obtained from 2D modeling can, however, be correlated to the 3D ones by introducing a correlation factor, Ramazani et al. [40] quantified by the stress ratio (σ_{3D}/σ_{2D}) based on the 2D and 3D RVE calculations for DP600 steels with various martensite phase fractions ($V_m=0-50\%$) at different equivalent plastic strains varying from $\epsilon_{eq}^p=0$ to 0.1. The correlation is a polynomial equation containing terms for both the martensite fraction and the equivalent plastic strain (7). In this way, the 3D flow stress of the studied steels was calculated from the 2D stress using:

$$\begin{aligned} \sigma_{3D}/\sigma_{2D} = & 2 \times 10^{-4} \times (\epsilon_{eq}^p)^2 \times V_m^3 - 1 \times 10^{-7} \times (\epsilon_{eq}^p) \times V_m^3 \\ & + 1 \times 10^{-7} \times V_m^3 + 0.0218 \times (\epsilon_{eq}^p)^2 \times V_m^2 \\ & - 0.0015 \times (\epsilon_{eq}^p) \times V_m^2 + 7 \times 10^{-5} \times V_m^2 \\ & + 0.18 \times (\epsilon_{eq}^p)^2 \times V_m + 0.007 \times (\epsilon_{eq}^p) \times V_m \\ & + 0.0036 \times V_m \times (\epsilon_{eq}^p)^2 + 1 \end{aligned} \quad (7)$$

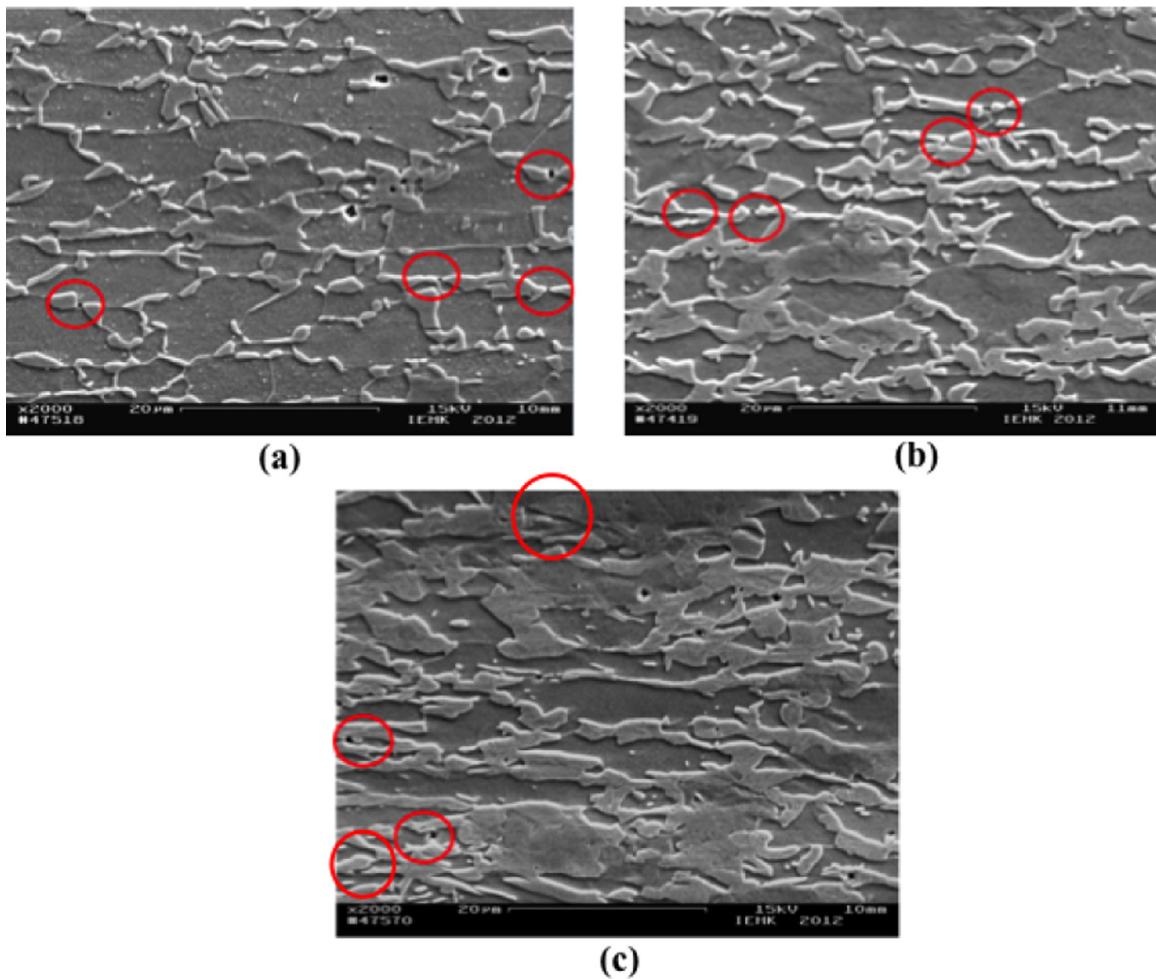


Fig. 6. SEM microstructure of DP600 steel with various amounts of martensite after tensile test. (a) 20% martensite, (b) 37% martensite and (c) 46% martensite. Crack initiation sites are in martensite, as indicated by red circles. The raised areas in the images are martensite. (For interpretation of the references to color in this figure, the reader is referred to the web version of this article.)

4. Results and discussion

4.1. Quantification of DP microstructure

As-received microstructures of the studied DP500, DP600, DP800 and DP1000 steels are depicted in Fig. 1. Based on image analyses using Digimizer software, the volume fraction of the martensite phase as well as the ferrite grain size were determined for each steel (Fig. 2). The results are presented in Table 3. The results for DP600 steel in Table 3 are for three different microstructures after various heat treatment conditions (Fig. 3). Table 3 shows that DP600 steels with higher austenization temperatures, have higher martensite volume fractions (Fig. 4).

4.2. Quantification of crack initiation

Under a tensile deformation, the DIC method was used to measure the strain distributions at each stage of deformation as well as the critical failure strain for all of the studied DP600 steels. The strain distribution was initially homogenous, but became non-homogenous in the final stages of deformation at which necking and fracture occurred. The strain distribution relevant to the fracture initiation for DP600 steel with 46% martensite is presented in Fig. 5a.

The local strain as a function of distance along the long central axis of the sample, illustrated in Fig. 5a, is presented in Fig. 5b. The

strain at which the curve changes abruptly was considered to be the critical failure strain, and the values for DP600 steels are presented in Table 4.

Combining these local strain values with the SEM analysis along the centerline, as shown in Fig. 5a, allows the matching of failure initiation position and local strain in the center of deformed specimen. Metallography inspections on the center line along the loading direction in the investigated DP steel revealed that for the steels examined here, martensite cracking was the primary mechanism of fracture and that failure initiated in martensite phase. SEM microstructures for the studied DP600 steels with various amounts of martensite are presented in Fig. 6. Fracture initiation sites are marked with red circles.

Figs. 6 and 7 show that cracks initiate from the martensite phase in laboratory generated DP600 steels and industrially produced DP500, DP800 and DP1000 steels respectively. As can be observed in these figures, the dominant failure initiation mechanism in all investigated DP steels is martensite cracking. In order to be assured that martensite cracking is the main reason for fracture, an in-situ bending test was also carried out and the microstructure was investigated during bending. The load-deflection curve in the bending test of DP600 steel with 46% martensite is depicted in Fig. 8. Small drops in the curve correspond to pauses in the experiment in order to capture SEM images. SEM images at the start of the test and after different displacements of DP600 steel with 46% martensite are shown in Fig. 8a. The inferences drawn

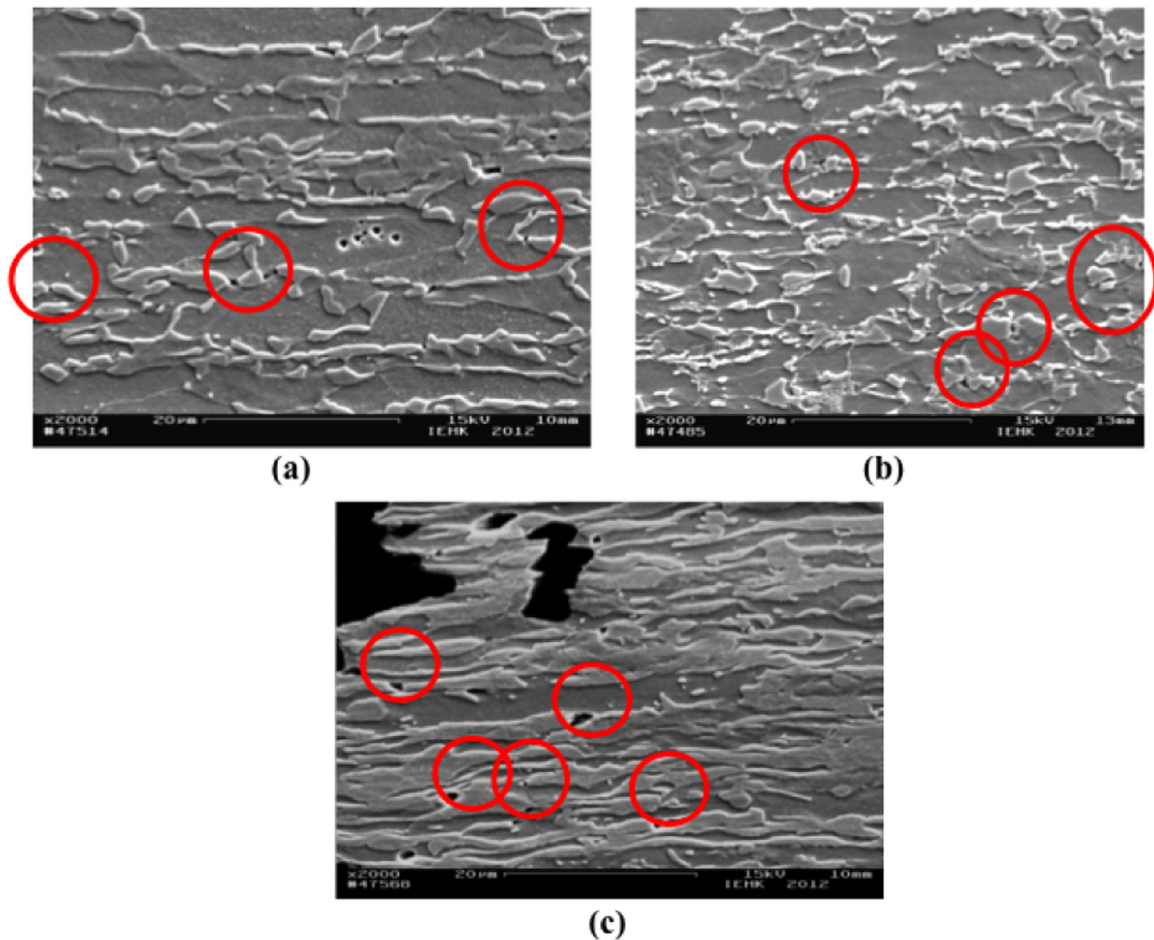


Fig. 7. SEM microstructure of industrially produced DP steels after tensile test: (a) DP500, (b) DP800, and (c) DP1000 steel. Crack initiation sites are in martensite, as indicated by red circles. The raised areas in the images are martensite. (For interpretation of the references to color in this figure legend, the reader is referred to the web version of this article.)

from these images are confirmed by EBSD measurements (Fig. 8b). Comparing the Kernel average miss-orientation (KAM) map (Fig. 8b) before and after the in-situ bending test showed that the crack nucleation occurred in martensite phase. The developed microcracks can be seen as black regions inside the martensite particles.

4.3. Micromechanical modeling

Rodriguez's approach [47], as discussed in Section 3.2, is used to develop the flow curve of ferrite at room temperature for each studied DP steel (Fig. 9a). For the ferrite phase in DP600 annealed at different temperatures, the disparities between the flow curves are marginal. Fig. 9a also shows the calculated flow curve of ferrite in DP500, DP800 and DP1000 steels.

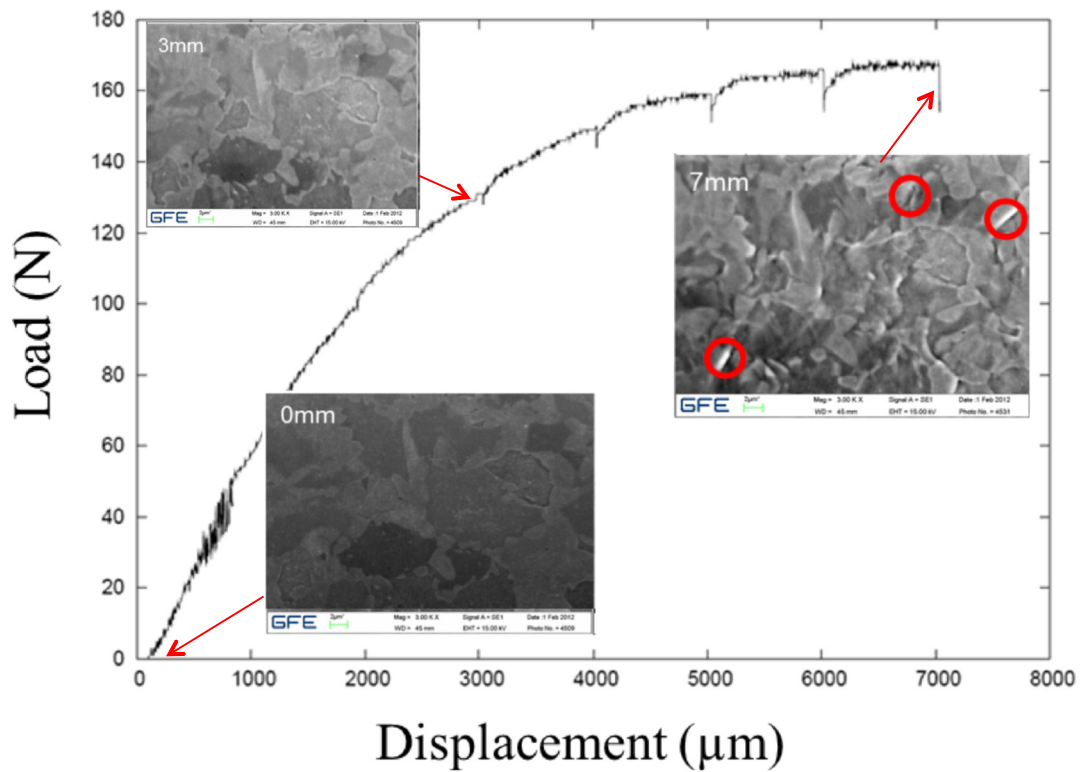
Taking the martensite fracture as the main mechanism for failure of DP steels during deformation, and applying the traction separation law as the fracture criterion, the RVEs of three studied DP600 steels were elongated uniaxially numerically up to the critical failure strain and the corresponding strain and stress of the martensite was obtained (Table 3). The fracture stress of martensite was obtained from the flow curve of martensite (Fig. 9 b). The martensitic flow curves are shown in Fig. 9b. For DP600 steel, the dissimilarities between the flow curves of martensitic phases annealed at various temperatures are considerably significant in comparison with the ferrite flow curves. The calculated stress-strain behavior of the martensite phases of the DP500, DP800 and DP1000 steels are also demonstrated in this figure. The increase of

the strength of the martensite flow curve is primarily due to increase in the carbon content. The martensitic flow curve of the DP500 steel is greater than the DP600 steel due to the fact that the carbon content of martensite for the chemistry of the investigated DP500 steel is higher than the martensite carbon content of the studied DP600 steels with various amounts of martensite fraction in this research work. For the carbon content in martensite, please refer to Table 3, where the austenite carbon content is reported. (During cooling after intercritical annealing, the austenite transforms to martensite with the same carbon content).

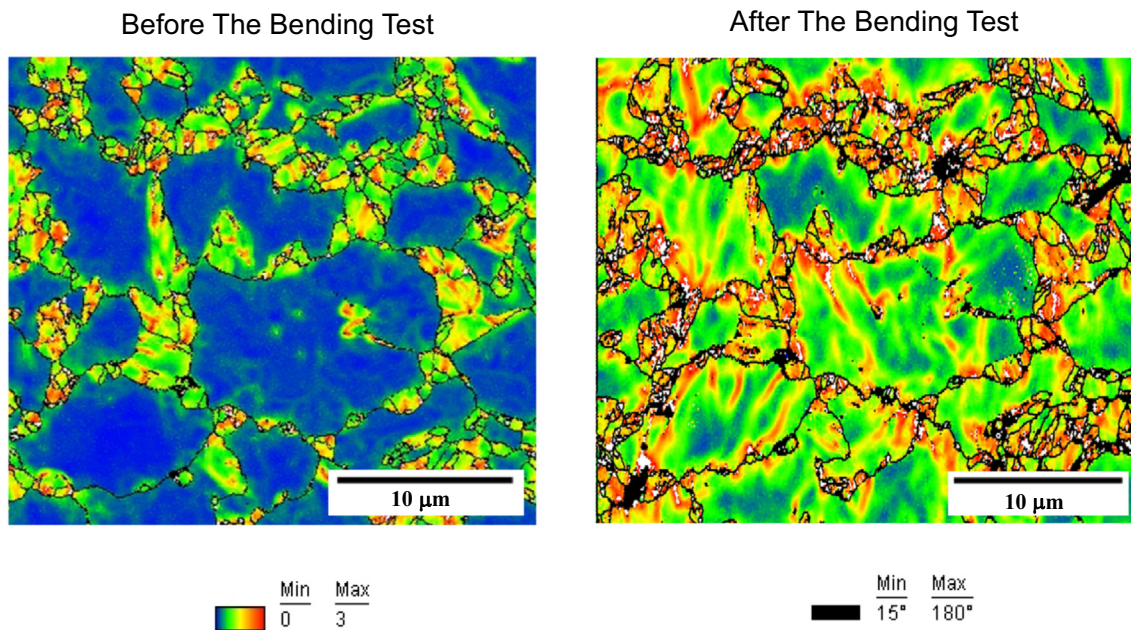
4.4. XFEM parameters identification

In Fig. 10, simulation results for stress and strain distributions in RVE of DP600 steel with 46% martensite volume fraction are presented. The simulations for DP600 steels were conducted up to the local failure strains determined from the experiments. Then, using first order homogenization strategy, the average equivalent plastic strain in martensite at the critical strain in the RVE was estimated.

The corresponding stress for this strain can be considered as the critical stress for martensite cracking in DP600 steel and it was calculated from the numerical flow curve of martensite based on Eq. (2) (e.g. $\sigma_c = 1525$ MPa for DP600 steel with 46% martensite). In J integral theory [57], the critical energy (E_c) for martensite failure is taken as the area below the martensite stress-strain curve. The critical stress and energy for the studied DP600 steels are listed in Table 4. The relevant data for all DP600 steels were obtained and



(a)



(b)

Fig. 8. (a) Load-deflection curve resulted from bending test for DP600 steel with 46% martensite, (b) microstructures and related KAM analysis maps relating to various amounts of displacements are also presented. Fracture initiation sites are denoted with red circles. (For interpretation of the references to color in this figure legend, the reader is referred to the web version of this article.)

plotted on critical stress and energy graphs based on carbon content of martensite (Fig. 11).

Since the properties of martensite depend significantly on the carbon content, we developed two empirical equations to describe

the XFEM model parameters for martensite cracking in DP600 steels as a function of the perspective martensite carbon concentration in their structures. (Eqs. (8) and 9) show the critical stress and energy of martensite as a function of its carbon content,

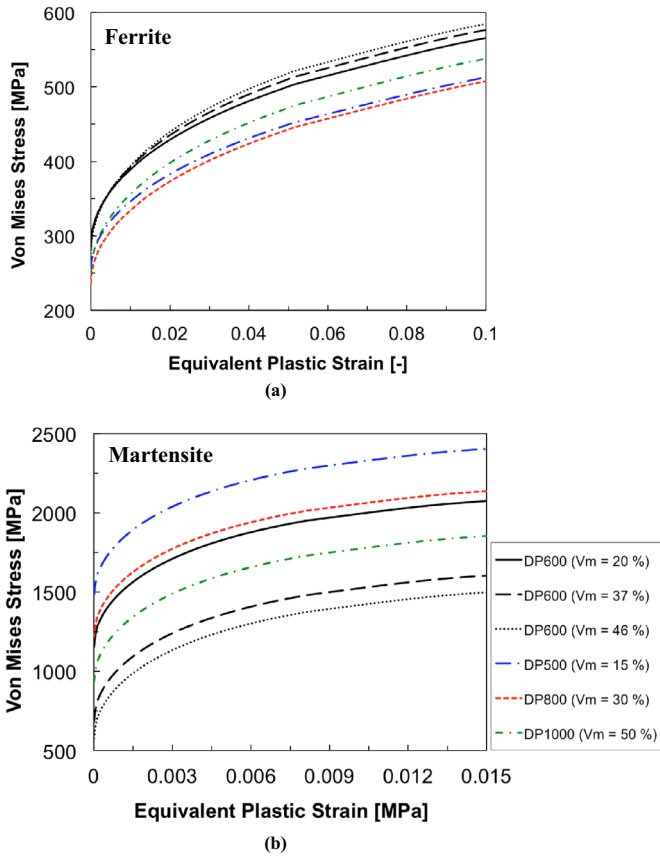


Fig. 9. Flow curves of (a) ferrite and (b) martensite regions of the studied steels. V_m here denotes the volume percentage of martensite.

respectively, based on fits in Fig. 11.

$$\sigma_c = 3230.9 \times \%C_{ss}^m + 1037.3 \quad (8)$$

$$E_c = 40.1 \times \%C_{ss}^m + 11.5 \quad (9)$$

It is deduced from Fig. 11 that (Eqs. (8) and 9) can be applied to determine XFEM model parameters of DP600 steels as function of their martensite carbon concentration. As it can be observed in Fig. 11, these relations imply that the critical stress and energy increase linearly with the carbon content of martensite carbon. In Fig. 11, the critical stress and energy of two other DP600 steels (DP600-2 [36] and DP600-3 [25]), obtained by other researchers, are presented as well in order to validate the developed equations.

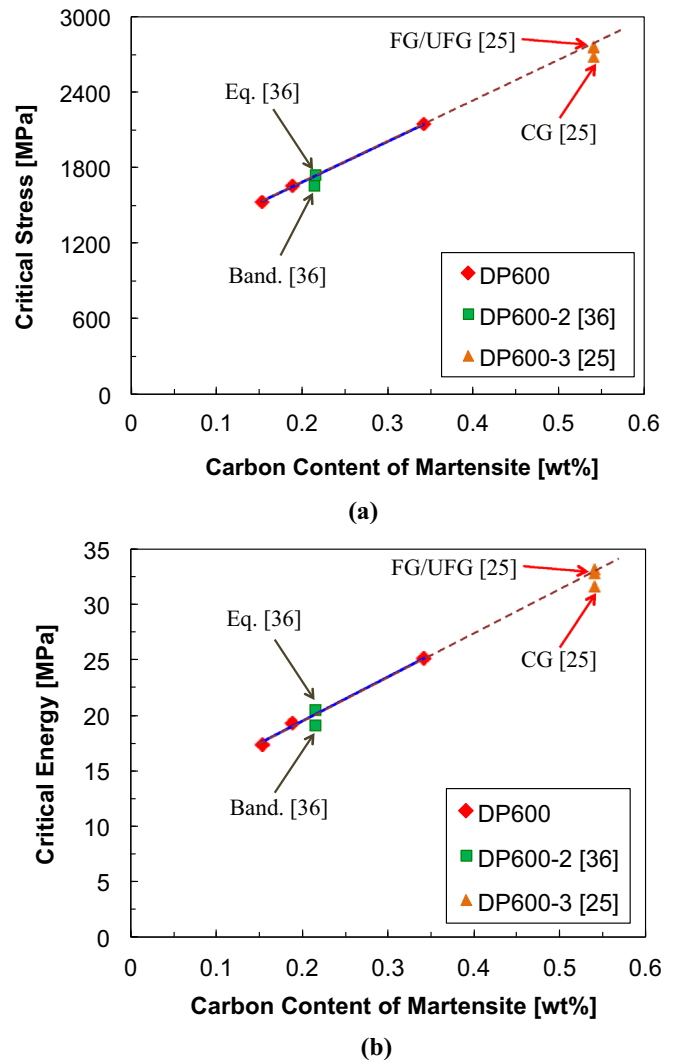


Fig. 11. Critical strength and energy graphs based on carbon content of martensite. DP600-2 and DP600-3 were respectively taken from Refs. [25,36] and parameterized to validate the developed approach. (For interpretation of the references to color in this figure, the reader is referred to the web version of this article.)

Green points in Fig. 11 show the critical stresses and energies for DP600-2 [36] with equiaxed and banded microstructures. Ramazani et al. [36] showed that failure initiation occurred in the DP600 steel with equiaxed microstructure in a higher plastic strain

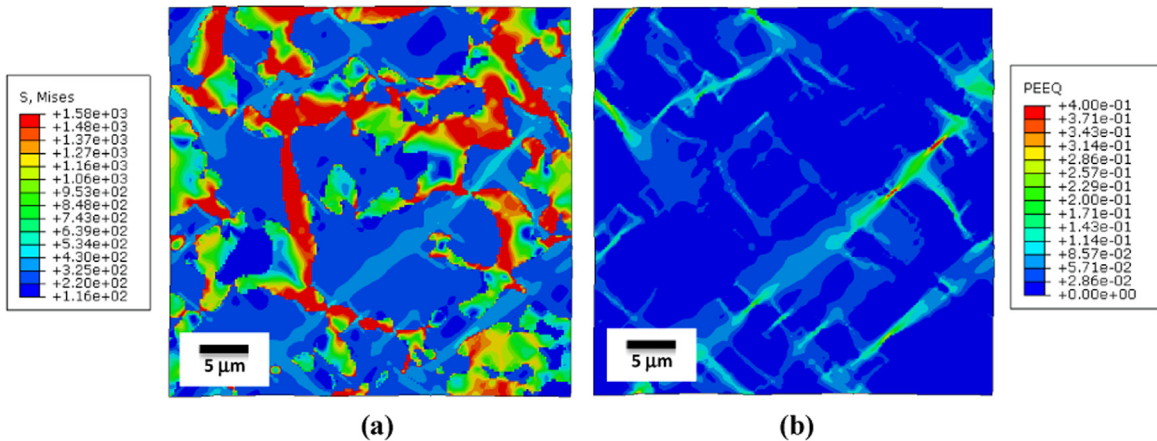


Fig. 10. Distribution of (a) Von Mises stress and (b) equivalent strain in RVE of DP600 steel with 46% martensite after stretching.

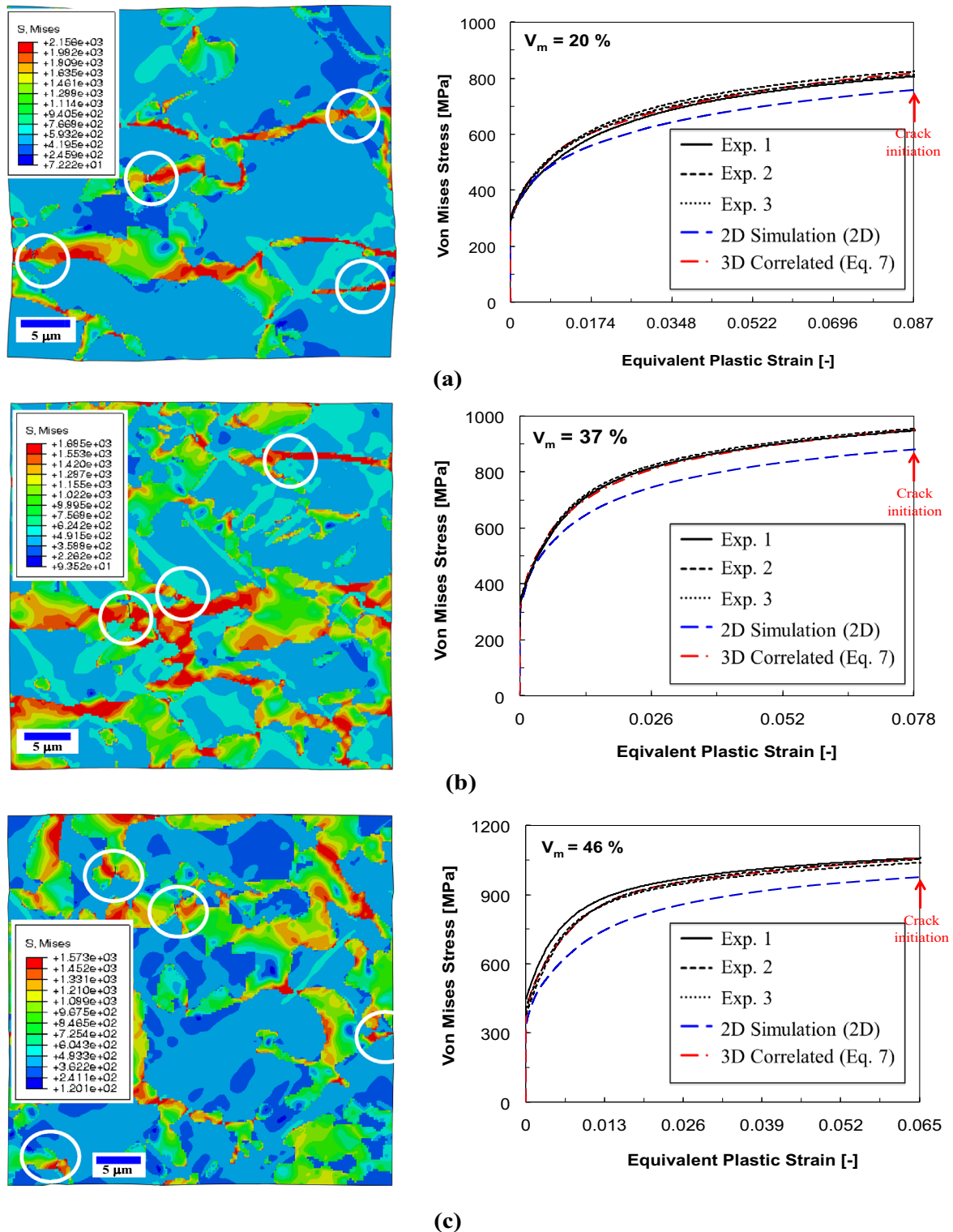


Fig. 12. Stress distribution and numerically obtained stress-strain curves of different DP600 steels, (a) 20% martensite (b) 37% martensite and (c) 46% martensite. Red and white circles show the crack positions. Stress distribution pictures relate to crack initiation strains indicated in stress-strain graphs. (For interpretation of the references to color in this figure legend, the reader is referred to the web version of this article.)

compared to the DP600 steel with banded microstructure. Therefore, the critical stress and energy for DP600 steel with equiaxed microstructure are higher than those for DP600 steel with banded microstructure, as can be seen in Fig. 11. However, they reported that martensite cracking is the dominant failure initiation mechanism independent of the morphology of the martensite. Since martensite carbon concentration in both

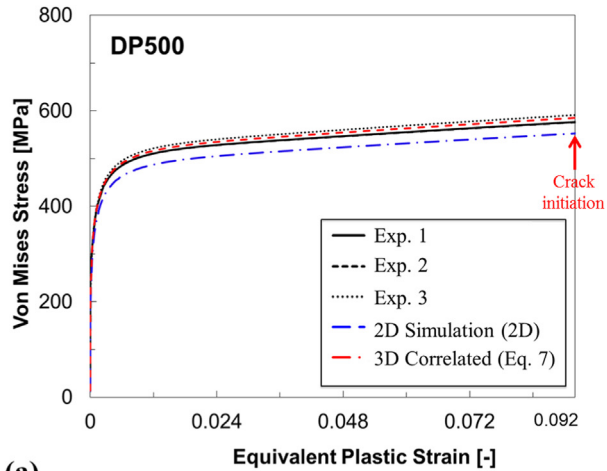
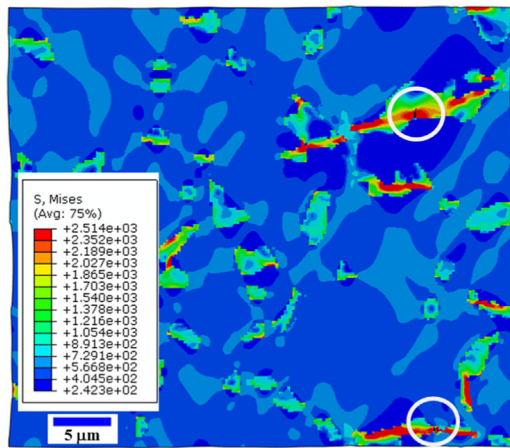
equiaxed and banded microstructures is almost the same (0.216 wt% for equiaxed microstructure vs. 0.215 wt% for banded microstructure), the same failure mechanism was observed in both structures [36], which is in good agreement with the fitted line on our investigated DP600 steels (Fig. 11).

The orange triangle points in this figure show the critical stresses and energies for DP600-3 [36] with coarse grain (CG), fine

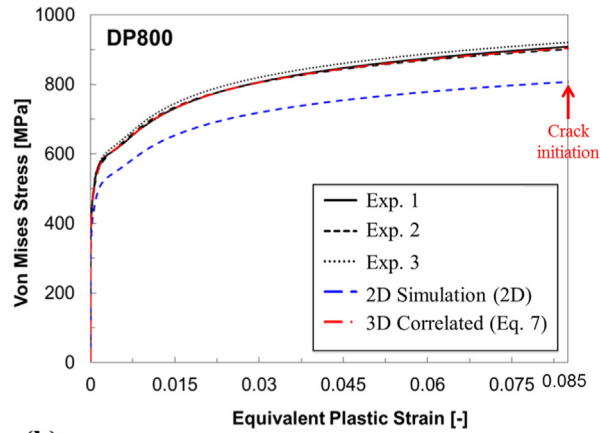
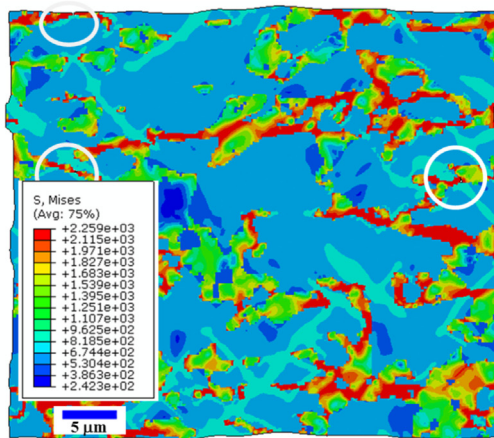
Table 5
XFEM model parameters identification for industrially processed DP grades.

Material	C_m (%)	$\sigma_c = 3230.9 \times \% C_{ss}^m + 1037.3$ [MPa]	$E_c = 40.1 \times \% C_{ss}^m + 11.5$ [J/m ²]
DP500	0.457	2514	29.77
DP800	0.378	2259	26.61
DP1000	0.281	1945	22.72

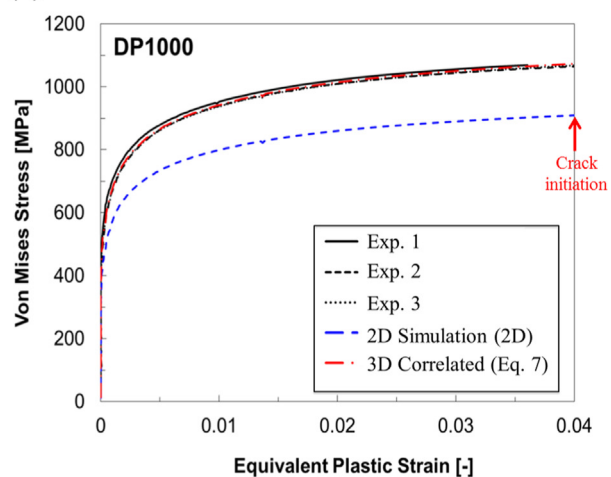
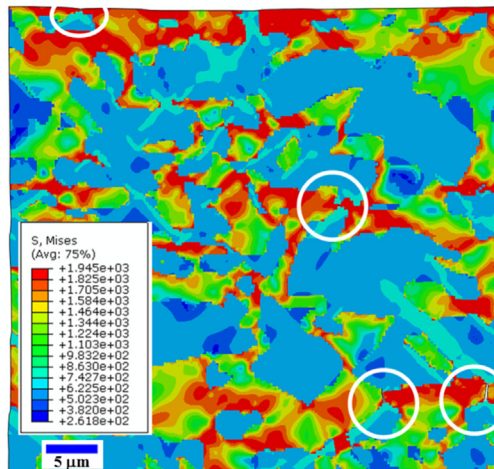
grain (FG) and ultrafine grain (UFG) structures. Calcagnotto et al. [23] reported that refining of the ferrite grains from 12 mm to 1.2 mm modified the tensile strength of DP600 steels. However, this refining of the grains showed insignificant effects on the ductility and failure strain of the material [23]. According to their statement, failure is caused by martensite cracking in coarse grained DP steels, while grain boundaries play the most significant role in the failure initiation of DP steels with fine and ultra fine ferrite grains. Ramazani [26] showed martensite cracking as well as ferrite/martensite debonding could occur in DP steels with fine



(a)



(b)



(c)

Fig. 13. Comparison between predicted and experimental flow curves for the different steels, (a) DP500, (b) DP800 and (c) DP1000.

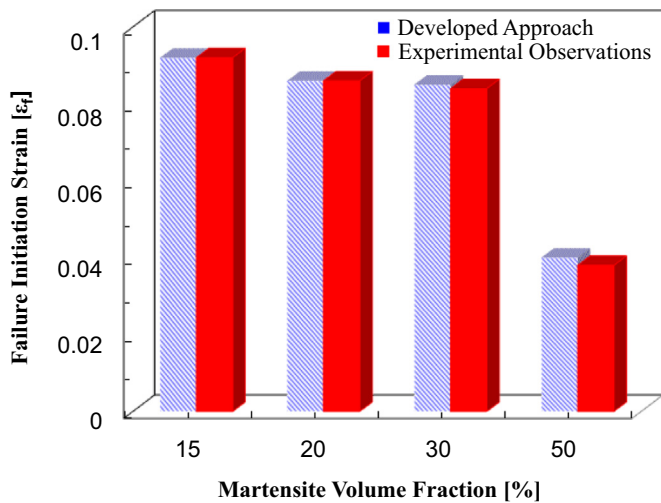


Fig. 14. Comparison between experimental and developed approach results for failure initiation strain of DP500, DP600, DP800 and DP1000 steels. DP steels are represented by martensite content according to Table 3.

and ultrafine grains. He [26] simulated martensite cracking in DP steels studied by Calcagnotto et al. [23], and found very good agreement between experimental and simulation results. He [26] calculated the same martensite carbon concentration in all Calcagnotto's materials with various ferrite grain sizes (0.54 wt% for all CG, FG, and UFG structures), which describes why ferrite grain size has a minor effect in the failure initiation mechanism in DP600-3 steels. Since martensite carbon concentration in all microstructures was almost the same, the same failure mechanism was observed in all structures [25], which is in good agreement with the fitted line on our investigated DP600 steels (Fig. 11).

4.5. Modeling of failure in DP600 steel using XFEM

In order to model the failure initiation in DP steels, XFEM was utilized. The onset and propagation of cracking in quasi-static problems were studied using the XFEM since it allows describing crack growth along an arbitrary, solution-dependent path without remeshing the FE model. After implementing XFEM on the martensite particles, numerical tensile tests were carried out on the generated 2D RVEs of DP600 steel. The evolution of stress and strain in the RVEs can be obtained from these numerical tensile tests. Fig. 12 illustrates the contour plot of von Mises stress and damage evolution on microscale at failure initiation strain (left hand side images) and a comparison between experimental for DP600 steels with (a) 20%, (b) 37%, (c) 46% martensite. The predicted true stress-true strain curves from 2D RVE calculations are demonstrated in the left hand side images of Fig. 12. The corrected 2D flow curve to 3D flow curve using correlation factor (7), as explained in Section 3.4, is also shown in this figure. As seen in Fig. 12, the corrected 3D flow curve is in excellent agreement with the experimental flow curve for the investigated DP microstructures. White circles in Fig. 12 show the cracked positions.

4.6. Generalization

It has been shown that martensite contributes to the plastic deformation and the main failure initiation mechanism is martensite cracking which has been modeled using XFEM within martensite islands. The analysis of the identified XFEM model parameters, namely critical stress and energy, allows an empirical equation as a function of local carbon content in martensite. The developed novel approach for cohesive zone model parameters identification was addressed for a series of DP600 steels with

various chemistries, martensite phase fractions, morphologies and ferrite grain sizes were presented in (Eqs. (8) and 9).

In order to validate the developed approach, it was applied for industrially processed DP grades with different chemistries and martensite fractions and strength levels. Since the failure initiation was occurred in martensite phase for all for DP500, DP800 and DP1000, as seen in Fig. 7. The XFEM parameters were calculated using (Eqs. (8) and 9) for these steel grades (Table 5).

Uniaxial numerical tensile tests were performed on the 2D RVEs for DP500 ($V_m=15\%$), DP800 ($V_m=30\%$) and DP1000 ($V_m=50\%$). Predicted flow curves from 2D RVE calculations were corrected to 3D flow curves using (7). The numerical results were compared with the experimental results in Fig. 13. As can be seen in this figure, the comparison of RVE calculated damage initiation in industrially produced qualities shows good agreement to experimental results. The simulations were conducted until the crack initiation took place in the RVE.

The failure strain was calculated as 0.092, 0.086, 0.085 and 0.04 for DP500, DP800 and DP1000 respectively (Fig. 13). For validation of these calculated failure initiation strain for studied DP steels, mini tensile test with DIC technique was carried out. Afterwards, SEM observations were performed on the broken samples along the central line according to the loading direction (Fig. 7). Based on experimental observations, the failure strain of 0.092, 0.086, 0.085 and 0.04 were identified for DP500, DP800 and DP1000, respectively (see Fig. 14). As shown in Fig. 14, a comparison between the predicted failure strain using developed approach and identified failure strain from experimental tensile test with DIC technique shows the developed approach can successfully predict the failure initiation strain DP qualities. Therefore failure initiation in components can be predicted for different DP steel qualities using a two-scale approach based on RVE calculation of the plastic hardening and failure of martensite.

5. Conclusions

1. In-situ bending test in SEM with EBSD measurements before and after the test were made to identify which phase or inter-phase fails first. Comparing the Kernel average miss-orientation (KAM) map before and after the in-situ test showed that the crack initiation occurs in the interior of martensite islands.
2. The local strain for failure initiation in DP steel that was obtained from the mini tensile test with the DIC technique was considered as a boundary condition in the RVE calculations. After simulation, the failure strain in martensite was identified using a first order homogenization strategy. The identified parameters were validated by comparing the predictions with experimental results for industrial steels.
3. SEM analysis was performed for pre-loaded DP samples with varying martensite contents. It was shown that martensite contributes to the plastic deformation and the main failure initiation mechanism is martensite cracking, which was modeled using XFEM within martensite islands. The determination of damage model coefficients by XFEM allows an empirical equation for XFEM parameters as a function of local carbon content in martensite to be determined. This approach was applied to industrially processed DP steel grades with varying strength levels. The comparison of RVE calculated damage initiation in industrially produced steels showed good agreement to experimental results.
4. Failure initiation in components can be successfully predicted for different DP steel qualities using the approach developed here, based on RVE calculation of the plastic hardening and failure of martensite.

Acknowledgements

This research was carried out under Project Number MC2.07293 in the framework of the Research Program of the Materials innovation institute M2i (www.m2i.nl).

References

- [1] A. Ramazani, K. Mukherjee, U. Prah, W. Bleck, *Comput. Mater. Sci.* 52 (2012) 46–54.
- [2] Y. Granbom, Ph.D. Thesis, KTH Royal Institute of Technology, Sweden, 2010.
- [3] P. Tsipouridis, Ph.D. Thesis, TU München, Germany, 2006.
- [4] A. Ramazani, B. Berme, U. Prah, *Structural materials and processes in*, in: D. Lehmhus, M. Busse, A.S. Herrmann, K. Kayvantash (Eds.), *Transportation*, Wiley-VCH, Weinheim, Germany, 2013, pp. 5–48.
- [5] R. Khamedi, A. Fallahi, H. Zoghi, *Int. J. Recent Trends Eng.* 1 (2009) 30–34.
- [6] A. Ramazani, P.T. Pinard, S. Richter, A. Schwedt, U. Prah, *Comput. Mater. Sci.* 80 (2013) 134–141.
- [7] A. Ramazani, K. Mukherjee, U. Prah, W. Bleck, A. Abdurakhmanov, M. Schleser, U. Reisgen, *Comput. Mater. Sci.* 68 (2013) 107–116.
- [8] World Auto steel, *Ultra-Light Steel Auto Body – Advanced Vehicle Technology (ULSABAVC) Programme, Overview Report*, January 2002. (www.elsab.org), 2002.
- [9] M. Pfestorf, *Great Designs in Steel Seminar*, BMW Group, 2005.
- [10] H. Qu, Master Thesis, Case Western Reserve University, USA, 2011.
- [11] ULSAB-AVC-PES Engineering Report, October 2001.
- [12] B.K. Zuidema, S.G. Denner, B. Engl, J. Sperle, *Soc. Automot. Eng.* (2011) 984–992.
- [13] M. Sarwar, R. Priestner, *J. Mater. Sci.* 31 (1996) 2091–2095.
- [14] H.P. Shen, T.C. Lei, J.Z. Liu, *Mater. Sci. Technol.* 2 (1986) 28–33.
- [15] L. Steinbrunner, D.K. Matlock, G. Krauss, *Metall. Mater. Trans. A* 19 (1988) 579–589.
- [16] Y.L. Su, J. Gurland, *Mater. Sci. Eng.* 95 (1987) 151–165.
- [17] A. Güral, S. Tekeli, T. Ando, *J. Mater. Sci.* 41 (2006) 7894–7901.
- [18] A. Ramazani, M. Abbasi, U. Prah, W. Bleck, *Comput. Mater. Sci.* 64 (2012) 101–105.
- [19] A. Ramazani, Y. Li, K. Mukherjee, A. Abdurakhmanov, U. Prah, M. Schleser, U. Reisgen, W. Bleck, *Mater. Sci. Eng. A* 589 (2014) 1–14.
- [20] E. Ahmad, T. Manzoor, K.L. Ali, J.I. Akhter, *J. Mater. Eng. Perform.* 9 (2000) 306–310.
- [21] A.F. Szewczyk, J. Gurland, *Metall. Trans.* 13 (A) (1982) 1821–1826.
- [22] G.R. Speich, R.L. Miller, TMS-AIME, Warrendale, PA, 1979, pp. 145–182.
- [23] X.J. He, N. Terao, A. Berghezan, *Met. Sci.* 18 (1984) 367.
- [24] J. Kim, G. Thomas, *Metall. Trans.* 12A (1981) 483–488.
- [25] M. Calcagnotto, Y. Adachi, D. Ponge, D. Raabe, *Acta Mater.* 59 (2011) 658–670.
- [26] A. Ramazani, Ph.D. RWTH-Aachen, Thesis University, Germany, 2013.
- [27] X. Sun, K.S. Choi, W.N. Liu, M.A. Khaleel, *Int. J. Plast.* 25 (2009) 1888–1909.
- [28] V. Uthaisangsk, U. Prah, W. Bleck, *Procedia Eng.* 1 (1) (2009) 171–176.
- [29] O. Cleizergues, T. Sturel, M. Difant, F. Mudry, *J. Phys. IV* 6 (1996) 195–204.
- [30] I. Scheider, *Procedia Eng.* 1 (2009) 17–21.
- [31] ABAQUS/Analysis user's manual Version 6.10, ABAQUS Inc.
- [32] N. Vajragupta, V. Uthaisangsk, B. Schmaling, S. Munstermann, A. Hartmaier, W. Bleck, *Comput. Mater. Sci.* 54 (2012) 271–279.
- [33] X.C. Zhuang, C. Xu, Z. Zhao, *Sci. China Technol. Sci.* (2015), <http://dx.doi.org/10.1007/s11431-015-5772-9>.
- [34] A. Ramazani, A. Schwedt, A. Aretz, U. Prah, *Key Eng. Mater.* 586 (2014) 67–71.
- [35] A. Ramazani, A. Schwedt, A. Aretz, U. Prah, W. Bleck, *Comput. Mater. Sci.* 75 (2013) 35–44.
- [36] A. Ramazani, Z. Ebrahimi, U. Prah, *Comput. Mater. Sci.* 87 (2014) 241–247.
- [37] A. Ramazani, Y. Chang, U. Prah, *Adv. Eng. Mater.* 16 (2014) 1370–1380.
- [38] C.C. Tasan, et al., *Annu. Rev. Mater. Res.* 45 (2015) 1–41.
- [39] M. Calcagnotto, D. Ponge, E. Demir, D. Raabe, *Mater. Sci. Eng. A* 527 (2010) 2738–2746.
- [40] A. Ramazani, K. Mukherjee, H. Quade, U. Prah, W. Bleck, *Mater. Sci. Eng. A* 550 (2013) 129–139.
- [41] ASTM E8/E8M-13a, *Standard Test Methods for Tension Testing of Metallic Materials*, ASTM International, West Conshohocken, PA, 2013.
- [42] P. Pinard, A. Schwedt, A. Ramazani, U. Prah, S. Richter, *Microsc. Microanal.* 19 (2013) 996–1006.
- [43] ASTM E562, *Standard Test Methods for Tension Testing of Metallic Materials*, ASTM International, West Conshohocken, PA, 2013.
- [44] W. Dahl, H. Rees, *Die Spannungs-Dehnungskurve Von Stahl*, Verlag Stahleisen, Duesseldorf, 1976.
- [45] L. Yang, L. Smith, A. Gotheke, X. Chen, *Auto/Steel Partnership*, Southfield, 2010.
- [46] J.R. Rice, *J. Appl. Mech.* 35 (1968) 379–386.
- [47] R.M. Rodriguez, I. Gutierrez, *Mater. Sci. Forum* 426–432 (2003) 4525–4530.
- [48] Y. Bergström, *Mater. Sci. Eng.* 5 (4) (1970) 193–200.
- [49] Y. Estrin, H. Mecking, *Acta Metall.* 32 (1) (1984) 57–70.
- [50] J.G. Sevillano, *Mater. Sci. Technol.* 6 (1993).
- [51] A. Ramazani, K. Mukherjee, A. Schwedt, P. Goravanchi, U. Prah, W. Bleck, *Int. J. Plast.* 43 (2013) 128–152.
- [52] A. Ramazani, K. Mukherjee, U. Prah, W. Bleck, *Metall. Mater. Trans. A* 43 (2012) 3850–3869.
- [53] N. Moës, J. Dolbow, T. Belytschko, *Int. J. Numer. Methods Eng.* 46 (1999) 131–150.
- [54] J.M. Melenk, I. Babuska, *Comput. Methods Appl. Mech. Eng.* 139 (1996) 289–314.
- [55] T. Belytschko, T. Black, *Int. J. Numer. Methods Eng.* 45 (1999) 601–620.
- [56] V.G. Kouznetsova, *Computational Homogenization for the Multi-Scale Analysis of Multiphase Materials* (Ph.D. Thesis), Technical University Eindhoven, The Netherlands, 2002.
- [57] G.E. Dieter, D. Bacon, *Mechanical Metallurgy*, McGraw-Hill, London, 1988.